Sensors and Actuators A 253 (2017) 188–197

Contents lists available at ScienceDirect

Sensors and Actuators A: Physical

journal homepage: www.elsevier.com/locate/sna

Multi-mode strain and curvature sensors for soft robotic applications

Edward L. White, Jennifer C. Case, Rebecca K. Kramer*

Department of Mechanical Engineering, Purdue University, 585 Purdue Mall, West Lafayette, IN 47907-2088, USA

ARTICLE INFO

Article history:
Received 16 June 2016
Received in revised form
17 November 2016
Accepted 23 November 2016
Available online 29 November 2016

Keywords:
Soft robotics
Soft sensors
Flexible sensors
Stretchable sensors
Liquid metal
Sensor arrays

ABSTRACT

In this paper we describe the fabrication and testing of elastomer-based sensors capable of measuring both uniaxial strain and curvature. These sensors were fabricated from Sylgard 184, which is a transparent silicone elastomer. We created microchannels directly in silicone elastomer substrates using a laser to ablate material. The sensing element was an alloy of gallium and indium, which is liquid at room temperature, contained within the laser-created microchannels. As the substrate deformed, the microchannel deformed within it, resulting in a measurable change in electrical resistance. By fabricating two matching resistive strain-sensing elements on opposite sides of the sensor, we were able to unambiguously measure uniaxial strain and curvature by observing the common mode and differential mode changes in resistance, respectively. There was very little coupling between modes, demonstrating the utility of the differential sensor design. We characterized the sensor in terms of its response to strain and curvature, its noise, and its stability over time. We believe that this type of sensor has application in soft sensory skins and can observe pose in soft robotic systems.

1. Introduction

Soft robotics is a new class of intelligent systems that move in ways very different than traditional rigid devices. Proposed applications of research in the field are roughly grouped into two related classes of soft robotic systems: mobile soft robots [1–4] and wearable robots [5,6]. Instead of being comprised of rigid joints and links, where motion is predominately localized at the joint, soft robots rely on continuum deformations to achieve motion [7–9]. This deformation is the source of the unique capabilities of soft robots. The drawback is that the distribution of deformation throughout the body significantly complicates the state observation problem. In order to achieve control of these soft systems, we must observe the current state [10–13]. In order to place sensors on the bodies of these systems, we need sensors which are materially compatible. Traditional sensors have high stiffness compared to the materials used in soft robots, necessitating the development of a new class of soft sensors made from the same low-stiffness materials found in the soft robots themselves.

In this paper, we present a multi-mode sensor which uniquely determines strain and curvature, as shown in Fig. 1. Our sensors were fabricated from Sylgard 184 silicone elastomer substrates containing microchannels filled with a gallium–indium alloy that is liquid at room temperature. Substrate deformation resulted in changes in the geometry of the liquid-metal-filled microchannels, resulting in a change in resistance. By measuring this change in resistance, we were able to determine the strain and curvature state of the sensor element. The liquid metal components described here and in previous work are strain sensors with an added stress concentrator to enhance their response to curvature. By combining two of these strain/curvature sensors, we demonstrate a device which can differentiate between positive curvature, negative curvature and strain. Individually, each element of the devices in this paper behaves according to the theory described in [14,15], which we revisit in our theoretical discussion below. In previously published devices, uniaxial strain and bending produced the same sensor output, resulting in ambiguous measurements. In the current case, the outputs from two sensing elements are used together to measure "common-mode" and "differential-mode" signals, which correspond to strain and curvature, respectively. The theoretical basis for this capability is described in a later section. In addition, the sensor described in this work is able to measure curvature without relying on a model of the underlying host object.

We anticipate that dual-mode strain and curvature sensors will be applicable across a wide range of soft systems, but will be particularly useful in thin devices such as soft sensory skins where significant strain and bending occur simultaneously. Our long-term goal is to develop multi-modal *active sensory skins*. In these devices, sensors and actuators are combined into a fabric or elastomer substrate which can then be attached to a deformable body to impart

---

* Corresponding author.
E-mail address: rebeccakramer@purdue.edu (R.K. Kramer).

http://dx.doi.org/10.1016/j.sna.2016.11.031
0924-4247/

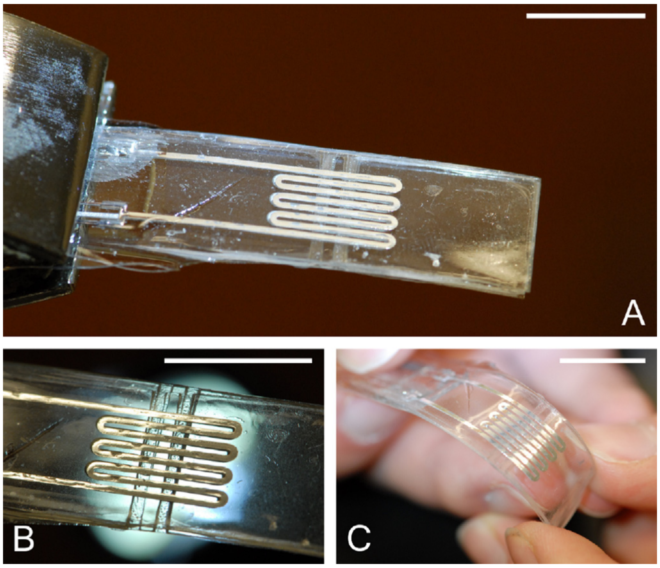

Fig. 1. Overview of a differential multi-mode sensor. (A) The top of the sensor. (B) The sensor with backlighting, highlighting the location of the stress concentrator channels behind the liquid-metal-filled microchannel. (C) The high deformability of the device resulting from the material properties of the elastomer substrate. The scale bar in the upper right corner of each figure is 6.25 mm.

motion. The sensor element presented in this work is one element which could be included in these future devices. In order to measure curvature across a surface, an array of curvature sensing elements, such as those discussed in this paper, would be required. The exact design of that sensor array would require an understanding of the spatial characteristics of the curvature field to optimize sensor placement. In a surface-based sensory array, only the deformed state of the surface of a deformable body will be known, and even with that the deformation field will only be known at the location of the sensors in the array. We suggest that boundary element methods from computational mechanics would be applicable to solving this problem, but this is outside the scope of the current work.

Elastomer-based sensors with encapsulated liquid metals such as those described in this work are well represented in the literature. Previously reported soft sensory devices based on elastomers substrates include joint angle and curvature sensors [14,15], pressure sensors [16,17] capacitance-based multi-element force sensors [18,19], liquid-metal/conductive fluid hybrid strain sensors [20–22], and multi-mode resistance-based devices measuring in-plane strain and out-of-plane pressure [23]. The current work furthers the previously developed devices by being able to differentiate between positive curvature, negative curvature and strain, while still being highly stretchable and capable of undergoing large deformations. Additionally, the current work is able to measure curvature without knowing the geometry of, or even requiring, an underlying host. This is in contrast to previous work which used deflection of a mechanical joint to induce strain in a liquid metal sensor, and required re-calibration on a per-host basis [14,15]. Finally, the current work expands upon the previous example of multi-layer liquid metal sensors by placing strain gauges in parallel, rather than orthogonally [23]. This allows us to measure curvature, while the previous work was used to measure biaxial strain. These sensing modalities could be combined in devices with even more sensor layers in the future.

Beyond elastomers, other types of materials can be used to sense curvature based on strain measurement. These include multilayer composites based on carbon film/polymer electrolyte [24], conductive polymers [25], and piezoceramic systems [26]. Extending even further, Bragg fiber gradings are another common curvature sensing modality [27–30]. Changes in magnetic field have also been used to measure curvature [11]. These approaches to sensing curvature provide a range of sensitivities and accuracy. Depending on the application, the relative importance of accuracy, repeatability, integration and stretchability will vary. We believe that elastomer-based, and in particular silicone-elastomer-based sensors, have the greatest potential for integration into active sensory fabrics and sensory skins due to their low stiffness, high stretchability, lack of rigid components, and chemical resistance.

2. Liquid metal embedded elastomer sensor body fabrication

The devices we present in this paper are soft, flat, transparent devices comprised of layers of patterned silicone elastomer. The complete device is shown in Fig. 1, which shows the liquid-metal-filled microchannels and stress concentrator features. The bodies of the devices were manufactured from Sylgard 184 (Dow Corning) film with gallium indium alloy (EGaIn, Sigma-Aldrich) filled microchannels. This configuration contained two strain gauges placed back-to-back. The devices described in this work were fabricated in four major steps: substrate preparation, substrate patterning, microchannel filling, and interfacing. The fabrication sequence is shown in Fig. 2.

Sylgard 184 (polydimethylsiloxane, PDMS) substrates were prepared by spin-coating the uncured polymer onto 3 in. × 2 in. glass slides (Fig. 2:A1 and B1). Before applying liquid polymer, a film of mold release (Ease Release 200, Mann Technologies) was applied to the slide. Four layers of elastomer were applied to achieve uniformity. These layers were applied at 500 rpm, and spun for 180 s using a Specialty Coating Systems Spincoat G3-8. The elastomer layers were allowed to cure for at least 4 h at 60° between applications. The resulting elastomer substrates were $273 \pm 8.25\ \mu m$ (95% confidence) as measured by a Zeta Instruments Zeta 20 3D microscope.

The blank substrates were patterned using a Universal Laser Systems VLS 2.30 laser system fitted with a 30W CO_2 laser operating at $10.6\ \mu m$ (Fig. 2:A2 and B2). The pattern created by the laser is shown in Fig. 3. This image contains a mixture of “thru” and “blind” features. Thru features are cuts made by the laser that pass completely through the elastomer layer into the glass substrate. Blind features only remove part of the thickness of the elastomer layer. The depth of the cut is controlled by adjusting laser power. Our approach of directly patterning features into the Sylgard 184 film is different than previously published approaches that used a mold to create channels. This direct approach has the advantage of not requiring the fabrication of a mold, which removes several processing steps and decreases design iteration time. However, the laser ablation process results in deposits of soot and debris on the surface of the substrate. Unless this material is removed, it interferes with bonding between elastomer layers. Further, small particles remaining in the microchannels can either cause wicking of liquid elastomer into the channel, resulting in a filled channel, or can block the channels themselves. For these reasons, a thorough cleaning process is required after patterning. First, the substrates were cleaned by sonication in a Liquinox detergent solution (Alconox) for 10 minutes in a Branson Bransonic 1800 bath ultrasonicator to remove the bulk of the soot left over from the patterning process. Second, we used a Kimwipe (Kimberly-Clark) with toluene to manually remove soot from the microchannels. We note that toluene aggressively swells Sylgard 184, and so the minimal amount required to wet the Kimwipe was used. Third, we sequentially rinsed the substrates in acetone, isoproponol, ethanol, and distilled water to remove film contaminants. Finally, we dried the clean patterned substrates at 60 °C to remove moisture.

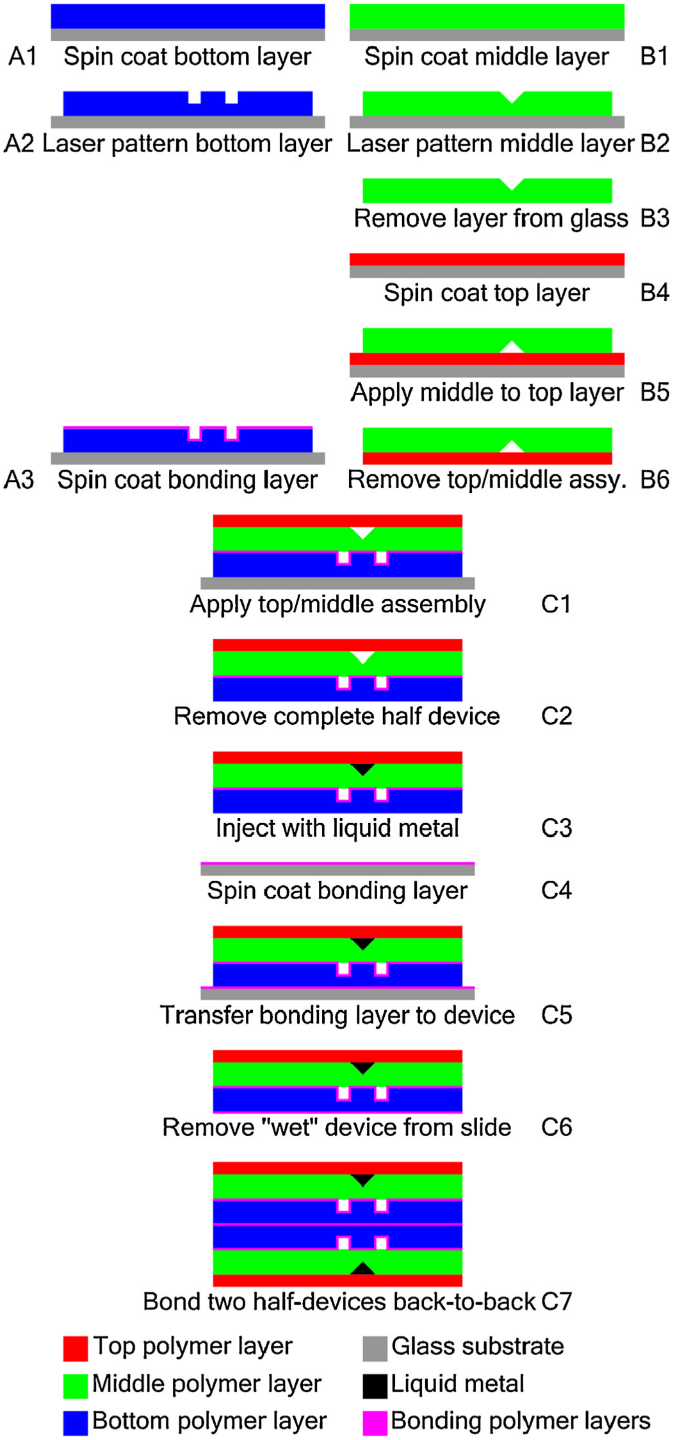

Fig. 2. Complete fabrication sequence. Steps A1–A3 proceed in parallel with steps B1–B6. Steps C1–C7 follow after A3/B6.

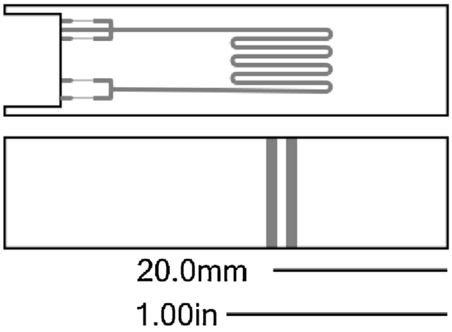

Fig. 3. Laser cut pattern. The upper image shows the “middle” layer with microfluidic channels. The lower shows the “bottom” layer with stress concentrator features. Black outline represents a complete vector cut through the material, gray regions are only partially ablated through the substrate. The two scale bars at lower left are 20.0 mm and 1.00 in. long, respectively.

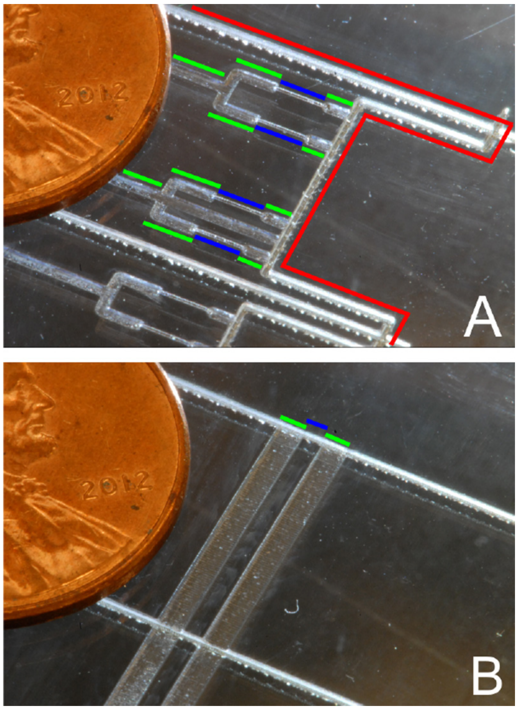

Fig. 4. Photographs of patterned Sylgard 184 elastomer film on glass substrate. (A) Shows three basic modes of laser patterning: through-film patterning (red highlight), thin feature (blue) and thick feature (green). Through-film and thin features were patterned using a continuous movement of the laser, similar to a plotter, while the thick features were patterned using pixel-based approach where the laser raster scanned over the surface. (B) Shows the ability of the laser to create boss features (green) by removing material around the feature (blue). (For interpretation of the references to color in this figure legend, the reader is referred to the web version of this article.)

Once cleaned, we measured the geometry of the laser-cut features using a Zeta Instruments Zeta 20 3D microscope. Since the materials involved in this study were soft, a non-contact (i.e. optical) method was selected to perform the characterization. There were two types of features created by the laser system: raster and vector patterns, as shown in Fig. 4. These patterns only differed in the way the laser was actuated. In raster-mode, the laser sweeps back and forth, pulsing the laser when it passes over a spot to ablate the surface. In vector mode, the laser moves like an XY-plotter, tracing a continuous path over the surface while the laser pulses. The impact of these two modes is manifested in the roughness of the resulting feature. Vector mode results in a smoother feature than raster mode. However, for features requiring larger lateral dimensions than a single laser spot, raster mode must be used. Thus, vector mode is used for thin microchannels, while raster mode is used for the wider microchannels, fill ports and stress concentrators. The cross sections, along with measured dimensions, are shown in Fig. 5. The letters in parentheses in the following sentence refer to the labels in that figure. Over all the sensors fabricated for this study, the depth of the stress concentrator (B) 156 ± 10.4 μm, the width (C) was 1323 ± 40.0 μm and the pillar

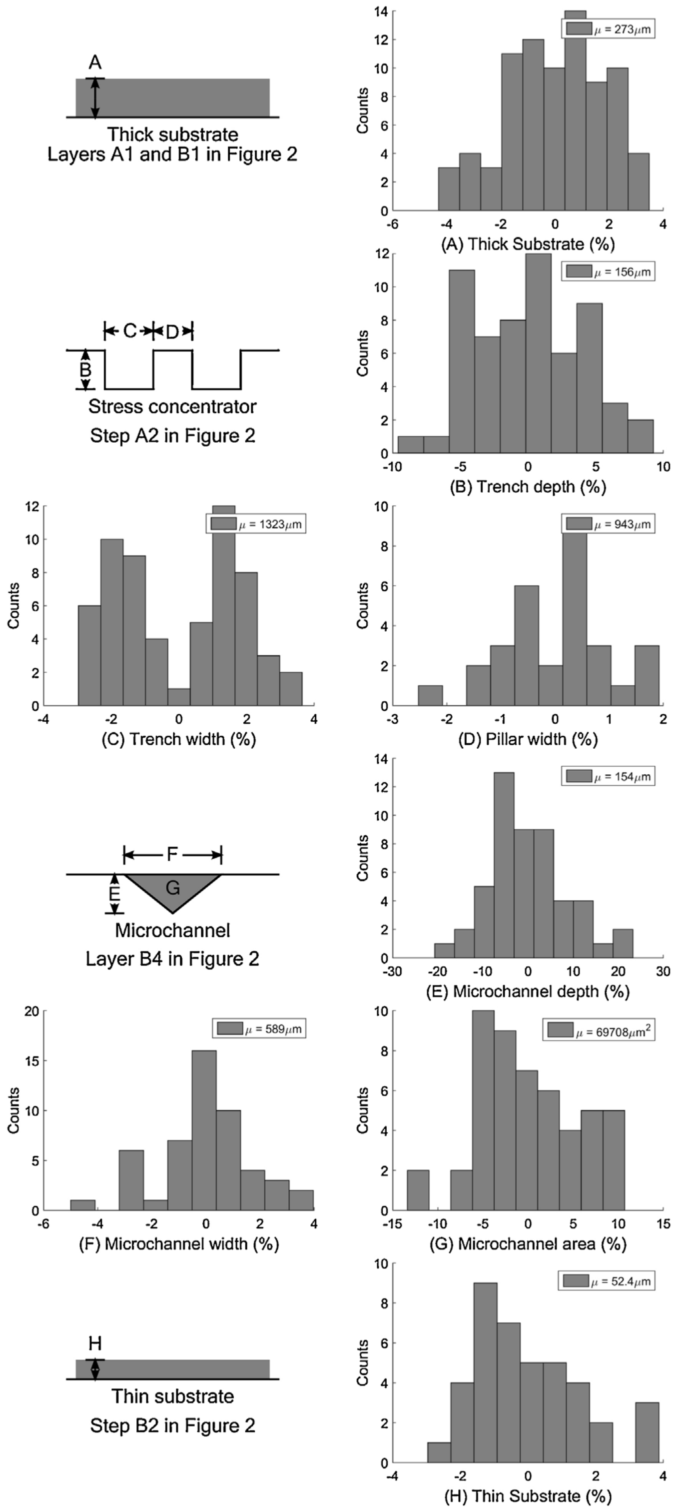

Fig. 5. Histograms showing manufacturing variation associated with laser-manufacturing parameters. All histograms show deviation from mean as a percentage, with the mean (μ) reported in the box in the upper right in μm. The top row shows the data for the thick elastomer substrates. The second and third rows show data from the features generated by the laser in raster mode. The fourth and fifth rows show data from the features generated in vector mode. The sixth row shows data for the thin elastomer substrate.

width (D) was 943 ± 16.0 μm. For the microchannels, the depth (E) was 154 ± 22.8 μm, the width (F) was 589 ± 17.3 μm and the cross sectional area (G) was 69,700 ± 6700 μm^2. All bounds represent 95% confidence intervals.

After measurement, the patterned "middle" layer was removed from the glass slide and cleaned again in acetone, isoproponal, ethanol, and distilled water to remove mold release from the back side of the substrate (Fig. 2:B3). To fabricate the top layer, we prepared another blank PDMS substrate by coating a glass slide with mold release, and spinning a layer of Sylgard 184 onto the slide at 500 rpm for 180 s (Fig. 2:B4). This resulted in a layer 52.4 ± 1.42 μm thick, as measured by a Zeta Instruments Zeta 20 3D microscope. We placed this in an incubator at 60 °C for ≈50 min, until it was "tacky." At this point, we placed the middle PDMS layer, patterned side down, onto the tacky PDMS, effecting a strong bond between the layers (Fig. 2:B5). Curing overnight in an incubator at 60 °C finalized the bond. We used the "tacky" bond approach instead of the more traditional plasma-based approaches due to poor bonding between laser-patterned layers of Sylgard 184 with plasma. This approach has been described previously [31].

To bond the middle/top layer assembly to the bottom layer, we applied a thin layer of liquid PDMS to the bottom layer through spin coating at 2000 rpm for 180 s (Fig. 2:A3). The middle/top layer assembly was placed on top of the wet bottom layer, pressed into place to remove bubbles, and placed in an incubator at 60 °C overnight to cure (Fig. 2:C1). This process resulted in a three-layer stack that comprised one half of the complete device.

After curing, we removed the completed subassemblies from the glass substrates (Fig. 2:C2). We injected liquid gallium indium alloy using a syringe into the micochannels between the top and middle layers (Fig. 2:C3). We inserted stripped 34 ga copper wires into the injection ports to provide an electrical interface with our measurement equipment. Finally, to seal the wires to the devices and to fully encapsulate the liquid gallium indium, we poured a small amount of uncured Sylgard 184 over the back of the device, and cured it in an incubator at 60 °C.

Once each subassembly was completed, we tested the resistance of the sensor element. Subassemblies found to be functional (i.e. all four leads were connected) were combined into full devices, as shown in Fig. 1. To bond the two halves of the device together, we spun a thin layer of liquid Sylgard 184 onto a clean glass slide at 2000 rpm for 180 s (Fig. 2:C4). We placed the halves, side to be bonded down, onto this slide to "wet" the bonding side, and then removed them from the slide (Fig. 2:C5 and C6). Thus wetted, the two halves were aligned and pushed together, placed under a weight, and placed in an incubator at 60 °C overnight to cure (Fig. 2:C7).

In order to improve the stability of the sensors, during these tests we bonded Sylgard-184-infused muslin fabric squares to the ends of the device. There were two purposes for these reinforcements. The first was to stabilize the electrical interface by encapsulating the lead wires. The second was to better distribute the force into the body of the sensor. Preliminary testing showed that stress concentrations caused by handling the sensors caused a marked increase in variability. These reinforcement pads were only required during these tests because of the isolated nature of the sensors during testing. When implemented, the sensors would likely be integrated into a larger sensory skin, changing the requirements on the interface.

3. Electrical interface and characterization

The devices presented in this paper rely on room-temperature liquid alloy of gallium and indium as a sensing element. This liquid is embedded in microchannels within an elastomer matrix. As the matrix deforms due to externally applied stress, the microchannels deform. This deformation results in a change in the resistance of the embedded liquid metal. In order to observe this effect, we measured the voltage drop across the resistor while supplying a constant 100mA current through the device. This "four terminal"

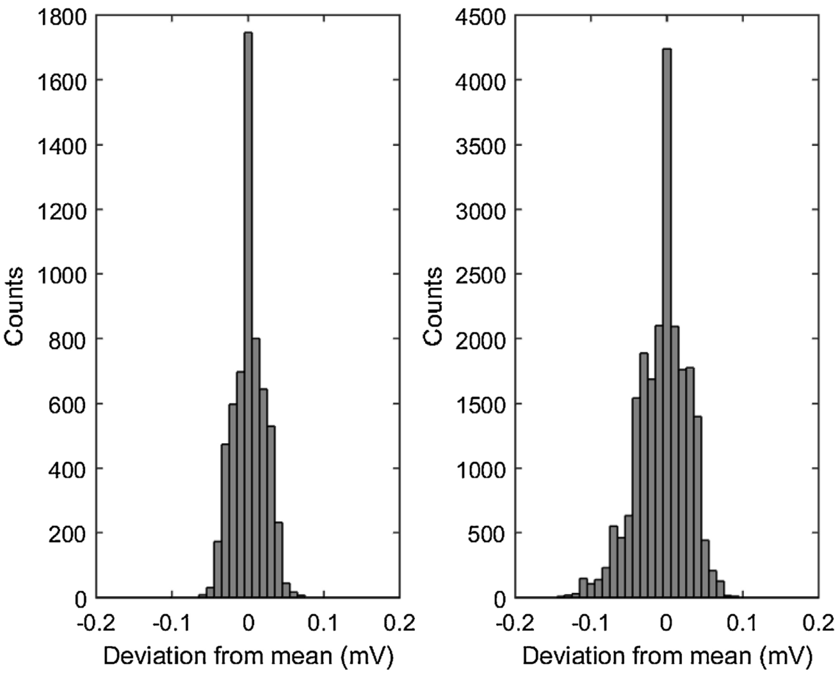

Fig. 6. Noise measurements of short and long time domains. The short time domain data represents 1000 samples captured at approximately 22 Hz across three sensors. The long time domain data represents 3600 samples captured at 1 Hz. Both sets of data are across all three sensors. The data reported show the deviation of observed values from the mode of all observations. The 95% confidence intervals are 0.0335 mV and 0.0546 mV, respectively.

measurement scheme allows us to negate the effects of interface resistance between electrical leads. Our selection of four-terminal versus the more common two-terminal measurement was motivated by a preliminary series of tests that indicated that the contact resistance was not only variable, but accounted for ≈10% of the total resistance. The electronics required for signal conditioning were designed and integrated onto a custom PCB, which we have described previously [32]. The sensitivity of the signal conditioning circuit is $0.0433\,\mathrm{V}\,\Omega^{-1}$. We measured the output from the signal conditioning electronics using an ADS1115 analog-to-digital converter (ADC) (Adafruit). This device allowed for differential voltage measurements with 16-bit resolution, combined with a programmable gain amplifier (PGA) on the device. The gain in the PGA of the ADC was set to 16, resulting in an overall resolution of the system of $0.00122\,\mathrm{V\,bit}^{-1}$ ($0.0282\,\Omega\,\mathrm{bit}^{-1}$).

One measure of performance is the noise in the sensor. To quantify the noise and drift in the sensor, we measured the unloaded response of the device in two time domains. The electronic noise measured in this process will be compared to the overall error in the sensor response in a later section. Compared to the uncertainty in the overall measurement, the electrical noise is a fairly small contribution to the overall error. We observed the high-frequency noise by sampling as rapidly as possible for 1000 samples, and observed the low-frequency noise by sampling at 1 Hz for 1 h. The measurement time and communication bandwidth effectively limited the high-frequency measurement to ≈22 Hz. This process used two different time domains to compare the effects of high-frequency noise, such as noise in the electronics and analog-to-digital converter, to the lower-frequency noise, such as thermal effects in the elastomer. The long-term measurements show a slightly larger deviation than the short term test, suggesting that there is a low-frequency component of the noise in addition to the high-frequency component. We speculate this could be due to thermal drift in the environment, as this test was conducted in ambient conditions. Further, these tests provide a noise baseline which we can compare to the sensitivity of the sensor in the next section. The distribution of observed values is shown in Fig. 6. The 95% confidence intervals of the short and long-term tests were 0.0335 mV and 0.0546 mV, respectively.

4. Strain and curvature sensing

We conducted two different types of mechanical tests on the sensors: curvature testing and uniaxial strain testing. All electrical measurements were made with the signal conditioning electronics described in the previous section. We tested the curvature response by wrapping the sensors around various solid cylindrical objects of known radius. The objects used in the study are shown in Table 1. In order to measure both positive and negative curvature, the sensors were flipped over and tested in both “up” and “down” configurations. We tested the strain response by stretching the sensor to known lengths. We marked two lines on the sensor body using a Sharpie permanent marker such that the insides of the lines were 20 mm apart. We placed a printed guide with lines 2 mm apart on a table surface. While looking through the clear Sylgard 184 body of the sensor, we extended it until the inside of the Sharpie lines matched the lines printed on the guide for a given extension. We tested extensions of 2 mm, 4 mm, 6 mm, and 8 mm. We found during testing that 10 mm extension, corresponding to 50% strain, caused unreliable operation and promoted failure. This

Table 1
Known diameters of cylindrical items used as known curvature objects. Measurements performed with hand-held digital calipers. The sensors were manually wrapped around these items to impose a known curvature.

Object	Known diameter and 95% confidence interval (mm)
1/2 in. PVC pipe	21.4 ± 0.157
1 in. PVC pipe	33.4 ± 0.0594
1 1/4 in. PVC pipe	42.1 ± 0.350
2 in. PVC pipe	60.4 ± 0.237
3D printed cylinder	79.4 ± 1.00

was likely due to separation of the liquid metal from the interface electrodes. Our previously published work has investigated the dynamics of the response of liquid-metal-based elastomer sensors, which showed that the response was generally decoupled from loading rate, and so we limit our experiments here to static loading conditions [33]. Each loading condition was tested three times in a random sequence which included both curvature and strain measurements. There were a total of 12 measurements of strain (4 conditions with 3 repetitions) and 30 measurements of curvature (10 conditions with 3 repetitions) for a total of 42 measurements per device. We fabricated three identical devices for this study. In the following sections, the data from all three devices is presented in aggregate, unless otherwise noted. Although we measured the voltage output from the two sensors, we were actually interested in the summation of these two signals, which we call sigma (Σ), and the difference between the output of the two sensors, which we call delta (Δ). These two derived responses are ideally only responsive to strain and curvature, respectively, while being insensitive to the other. In actuality, cross-coupling occurs due to variations in gauge factor.

Between each measurement, we returned the sensor to an unstrained state and took a baseline measurement. We report two different approaches to using this baseline resistance, which we call “averaged” and “updated.” In the averaged mode, only the initial and final baseline unstrained resistance measurements were used. We believe this is more representative of a case where a device might be zeroed at the beginning of operation, and then not returned to an unstrained state. In the updated mode, we used the baseline measurements before and after each measurement to compute the change in resistance. This more accurately reflects the dynamic response of the sensor, but the operation is less like a real-world application. Our previous work showed that liquid-metal-based devices are stable and respond primarily to strain, and do not experience stress relaxation effects [33]. To evaluate the stability of the devices, we compared the measured performance using the averaged and updated baseline approaches. This comparison is shown in Fig. 7, which shows data from the experiments described above. Based on these two figures, we see that there is no significant difference between using the average baseline resistance and continually updating the resistance. We believe this is a strong positive indicator to using these devices in practical soft systems.

We can analyze the output from the sensors by considering their resistance and basic mechanical properties. The resistance of a homogenous material is $R = \rho L/A$, where ρ is the resistivity of the material, L is the length, and A is the cross sectional area. Further, we can compute the volume of this same piece of material as $V = AL$, where V is the volume. If we assume that all of the materials are incompressible, $A = A_0L_0/L$, where the subscript indicates the initial condition. Substituting, the current and initial resistances are, $R = \rho L^2/A_0L_0$ and $R_0 = \rho L_0^2/A_0L_0$, respectively. We are interested in the change in resistance, and so we define:

$$\Delta R = R - R_0 = \frac{\rho}{A_0L_0}(L^2 - L_0^2) \tag{1}$$

The engineering strain in the sensor is defined as $\epsilon = L - L_0/L_0$. Substituting this into the proceeding:

$$\Delta R = \frac{\rho}{A_0L_0}((L_0(1+\epsilon))^2 - L_0^2) = R_0(2\epsilon + \epsilon^2) \tag{2}$$

Next, we define two values, Σ and Δ, which are the sum and difference of the outputs from the two sensors. This results in two measured properties:

$$\Sigma = GR_{0t}(2\epsilon_t + \epsilon_t^2) + GR_{0b}(2\epsilon_b + \epsilon_b^2) \tag{3a}$$

$$\Delta = GR_{0t}(2\epsilon_t + \epsilon_t^2) - GR_{0b}(2\epsilon_b + \epsilon_b^2) \tag{3b}$$

where G is the gain discussed in the previous section and the subscript t refers to the top sensor and b to the bottom sensor. Σ and Δ are the two quantities we are interested in, since they are very nearly decoupled from each other, and highly correlated to strain and curvature measurement, respectively. Next, we need to consider the strain in each sensor as a function of the loading condition. In the uniaxial strain case, the solution is trivial: $\epsilon = \epsilon_t = \epsilon_b$. Substituting these strains into the proceeding:

$$\Sigma_{\text{Strain}} = GR_{0t}(2\epsilon + \epsilon^2) + GR_{0b}(2\epsilon + \epsilon^2) = G(R_{0t} + R_{0b})(2\epsilon + \epsilon^2) \tag{4a}$$

$$\Delta_{\text{Strain}} = GR_{0t}(2\epsilon + \epsilon^2) - GR_{0b}(2\epsilon + \epsilon^2) = G(R_{0t} - R_{0b})(2\epsilon + \epsilon^2) \tag{4b}$$

In the case of curvature, we assume that the neutral axis of the deformation is in the middle of the sensor body, which is reasonable due to the symmetry of the device (see Fig. 2). The deformed length of the sensor element as a function of the curvature is:

$$L_t = \frac{L_0(r+T)}{r} \tag{5a}$$

$$L_b = \frac{L_0(r-T)}{r} \tag{5b}$$

where r is the radius of curvature to the neutral axis, and T is the thickness from the neutral axis to the plane of the sensor. The strains in the upper and lower sensors, along with the substitution of the proceeding, results in:

$$\epsilon_t = \frac{L_t - L_0}{L_0} = \frac{T}{r} = T\kappa \tag{6a}$$

$$\epsilon_b = \frac{L_b - L_0}{L_0} = -\frac{T}{r} = -T\kappa \tag{6b}$$

where κ is the curvature, defined as r^{-1}. We can substitute these expressions into Eq. (3):

$$\Sigma_{\text{Curvature}} = G(R_{0t} + R_{0b})(T^2\kappa^2) \tag{7a}$$

$$\Delta_{\text{Curvature}} = G(R_{0t} + R_{0b})(2T\kappa) \tag{7b}$$

Eqs. (4) and (7) represent the ideal response of the sensors. At this point, we assume that the initial resistance of all devices is similar. This is warranted since all of the sensor elements have nominally identical geometry. Making this assumption, the response due to strain and curvature becomes:

$$\Sigma_{\text{Strain}} = 2GR_0(2\epsilon + \epsilon^2) \tag{8a}$$

$$\Delta_{\text{Strain}} = 0 \tag{8b}$$

$$\Sigma_{\text{Curvature}} = 2GR_0(T^2\kappa^2) \tag{8c}$$

$$\Delta_{\text{Curvature}} = 2GR_0(2T\kappa) \tag{8d}$$

These theoretical relationships are shown Fig. 7 along with the experimental observations. As discussed previously, the devices are very thin. Therefore, we can neglect quadratic thickness terms. Further, if we linearize about zero strain, we are left with an approximate form that we recast as a system of equations:

$$\begin{bmatrix} \Sigma \\ \Delta \end{bmatrix} \approx 2GR_0 \begin{bmatrix} 2 & 0 \\ 0 & 2T \end{bmatrix} \begin{bmatrix} \epsilon \\ \kappa \end{bmatrix} \tag{9}$$

Since we are interested in determining the deformed configuration based on voltage measurements, we invert the system to obtain:

$$\begin{bmatrix} \epsilon \\ \kappa \end{bmatrix} \approx \frac{1}{4GR_0} \begin{bmatrix} 1 & 0 \\ 0 & \frac{1}{T} \end{bmatrix} \begin{bmatrix} \Sigma \\ \Delta \end{bmatrix} \tag{10}$$

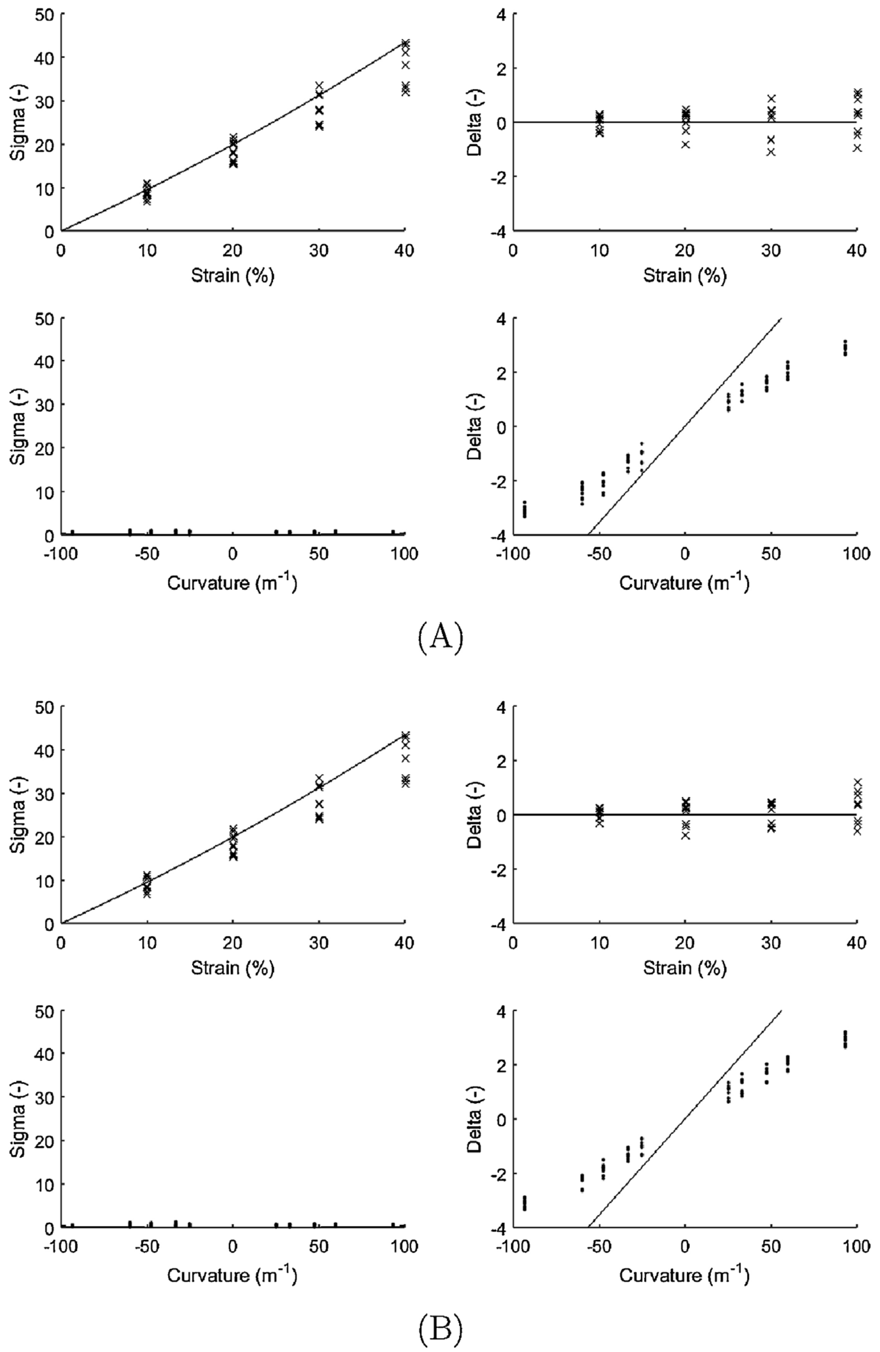

Fig. 7. Measured response of sensors to strain (top row) and curvature (bottom row). (A) Shows the response using the baseline resistance from the start and end of the test, while (B) shows the response with continual baseline updating. (A) is more representative of what would be observed in operation. The vertical axes show the sum (Σ) and the difference (Δ) of the signals from the upper and lower strain gauges. The solid lines show the theoretical response of the sensors based on Eq. (8). In this case, $GR_0 = 22.6$ mV and $T = 784$ µm. Both of these values were based on measurements across all of the devices used in the study. We suspect that the deviation between the deviation in predicted and actual value in the Δ response to curvature is due to elasticity of the sensor.

This expression demonstrates that this type of sensor has the capacity to simultaneously measure both strain and curvature. We would also like to point out that the assumption of identical initial resistance and the linearization step are not required to achieve this capability. Without the assumptions, Eq. (10) would be non-linear and contain four known initial resistance terms. As we show later, the capability of our sensors is limited by measurement noise, rendering this additional complication unnecessary.

Next, we wished to perform a regression analysis to quantify the response of the sensors. We began by assuming a linear response, which we believe is justified by Fig. 7, and the result in Eq. (10), of the form:

$$\epsilon = a_0 + a_1 \Sigma + a_2 \Delta \tag{11a}$$

$$\kappa = b_0 + b_1 \Sigma + b_2 \Delta \tag{11b}$$

where ϵ is the strain, κ is the curvature, Σ is the sum of the outputs from the resistive strain sensors, Δ is the difference in the outputs, and a_i and b_i are coefficients of the fit. Since we had an

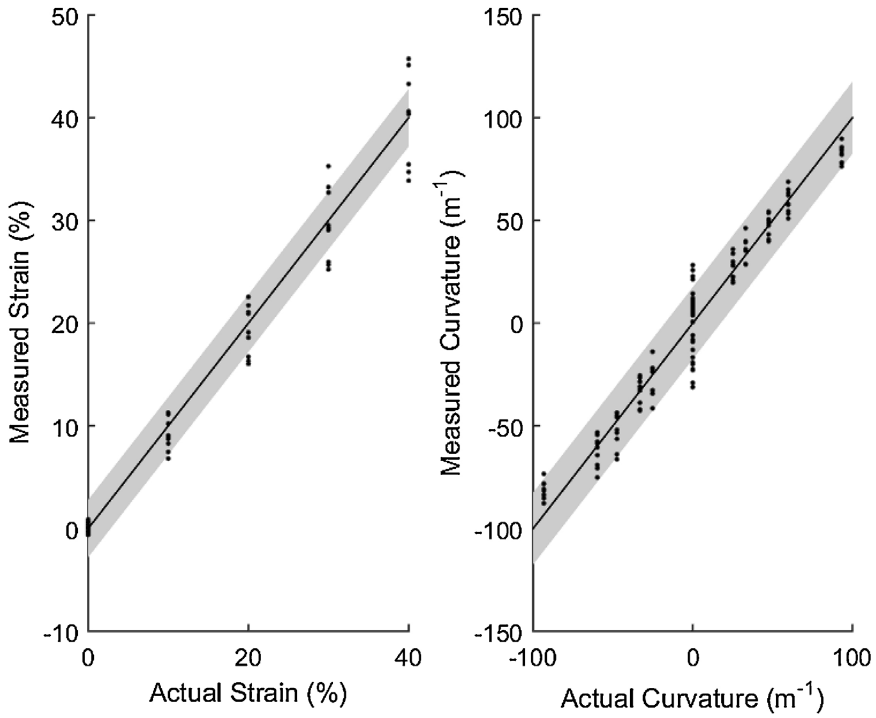

Fig. 8. Comparison of the known and measured strain and curvature in the left and right figures, respectively. The scattered points represent experimental observations, the shaded box represents the 95% confidence interval, and the solid line is an ideal 1:1 line. The errors between the experimental observations and ideal line are shown as a histogram in Fig. 9.

overconstrained system, we used a generalized least squares regression. To do so, we constructed a design matrix of the form:

$$\mathbf{D} = \begin{bmatrix} 1 & \Sigma_0 & \Delta_0 \\ 1 & \Sigma_1 & \Delta_1 \\ & \vdots & \\ 1 & \Sigma_i & \Delta_i \\ & \vdots & \\ 1 & \Sigma_{126} & \Delta_{126} \end{bmatrix} \tag{12}$$

where each row corresponds to a single measurement, and a response matrix of the form:

$$\mathbf{R} = \begin{bmatrix} \epsilon_0 & \kappa_0 \\ \epsilon_1 & \kappa_1 \\ & \vdots \\ \epsilon_i & \kappa_i \\ & \vdots \\ \epsilon_{126} & \kappa_{126} \end{bmatrix} \tag{13}$$

The system of equations we wished to solve was therefore:

$$\mathbf{DC} = \mathbf{R} \tag{14}$$

where **C** is a matrix of the unknown coefficients. Using a pseudo-inverse transformation, we determined the unknown coefficients:

$$\mathbf{C} = \begin{vmatrix} -0.399 & 3.86 \\ 1.07 & -0.169 \\ 0.124 & 27.6 \end{vmatrix} \tag{15}$$

We note that these coefficients assume strain in units of %, curvature with units of m^{-1} and voltages in mV. These are the same units shown on the corresponding figures.

In order to determine the quality of this model, we used Eq. (14) and the values of the coefficients in Eq. (15) to determine the estimated strain and curvature for each measurement. We have plotted these results in Fig. 8. Additionally, we have plotted histograms of the error between the experimental data and reconstructed data in Fig. 9. Based on this distribution, we found that the 95% confidence intervals for strain was 2.80% and for curvature was 17.5 m^{-1}. These two values corresponded to 7.00% and 8.75% of the full-scale of strain and curvature, respectively.

We previously stated that there was low coupling between the two measurements of strain and curvature. Looking at the coefficients in Eq. (15), the first row corresponds to the offset terms. The coupled terms (i.e. the strain response to Σ and curvature response to Δ) are C_{21} and C_{32}, respectively. These terms are $\mathcal{O}(1)$ and $\mathcal{O}(10)$. The cross-coupled terms are C_{22} and C_{31}. These terms are $\mathcal{O}(0.1)$ or less, which is one to two orders of magnitude lower than the coupled terms, demonstrating the low cross-coupling of the current device. Although this low cross-coupling is not a requirement of device operation, it greatly simplifies the overall functionality. In practice, the cross-terms could be eliminated, resulting in fewer mathematical operations to convert from resistance measurements to strain and curvature estimates.

Finally, we compared the model uncertainty to the noise measured in the system. The previously discussed noise and stability measurements were based on single channel measurements. To convert to two-channel measurements, such as our Σ and Δ parameters, we assumed independent, identically distributed noise. Under this assumption, we can combine noise from two channels using the root sum of squares, or $E_T = \sqrt{2E_1^2}$, where E_T is the total error, and E_1 is the error in a single channel. This resulted in a value of 0.0772 mV. Using the coupled terms in Eq. (15), we found this noise would result in variations of 0.0826% and 2.13 m^{-1} for

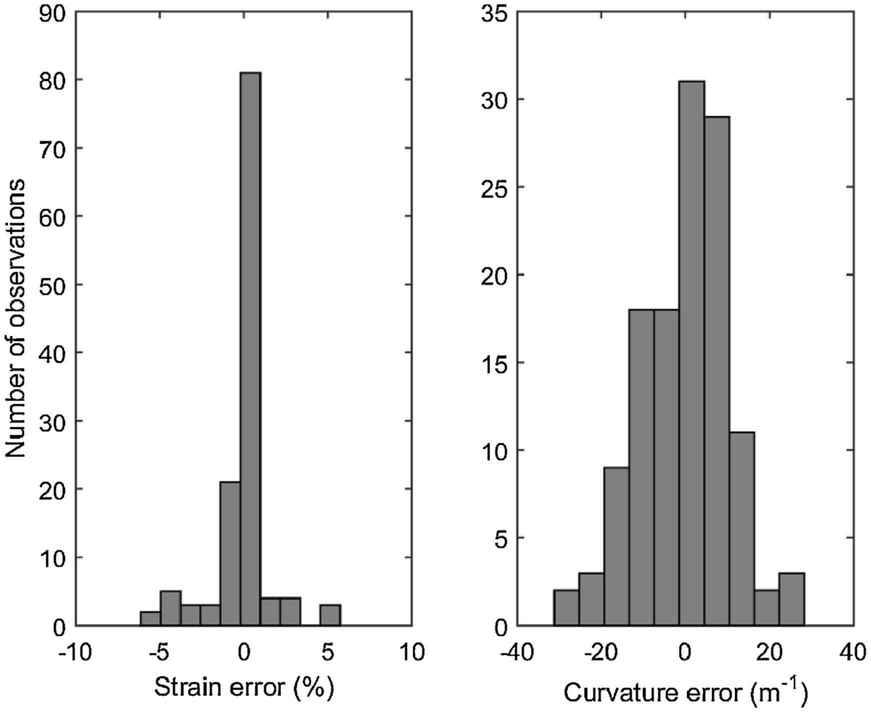

Fig. 9. Histogram of the error between the applied and measured strain and curvature. The histogram shows the distance from each observation to the ideal line in Fig. 8.

strain and curvature, respectively. These values are approximately an order of magnitude smaller than the uncertainty in the model, indicating that electrical noise is not a significant contributor to overall sensor performance.

In summary, the sensors exhibit good linearity and low coupling between summation and differential channels in response to strain and curvature. The electrical noise was a minor contributor to overall sensor performance. The primary limiting factor in sensor performance was scatter in the observed data, which we believe is primarily due to variation in how the sensors are held across different tests. Although the observed variation in the sensor is worse that what is expected in commercial strain sensors, the performance is acceptable for observing many soft systems.

5. Conclusion

As the soft robotics community continues to progress as a field towards more realistic applications and devices, we must become more tolerant of realistic loading cases. In our present study, we have fabricated a sensor that can measure both strain and curvature using soft materials that are compatible with soft robotic systems and wearable devices. The use of two coupled sensing elements allows the sensor presented in this work to differentiate between positive curvature, negative curvature, and strain. Previous curvature sensors required either knowledge of the kinematics of the host on which they were placed, or *in situ* calibration to translate strain into curvature. With this device, we use the difference in output from two paired resistive strain sensors to produce measurements of curvature and strain without requiring any knowledge of the host. In the future, this two-element sensor could be used as the basis for more complex soft robotic skins that are capable of measuring their state across their entire surface.

One of the challenges associated with wider adoption of this class of device is manufacturing. At the end of the fabrication sequence, the device consists of nine layers of silicone elastomer containing two different liquid metal filled microchannel structures (Fig. 2:C7). This results in a complex process with many steps and a low overall device yield rate. We intend to integrate our other research on manufacturing liquid metal-based stretchable electronics using approaches such as ink-jet printing to simplify the design and manufacturing processes.

Acknowledgements

This work was supported by the National Aeronautics and Space Administration under the Early Career Faculty program (NNX14AO52G). ELW is supported by the National Science Foundation Graduate Research Fellowship Program (DGE-1333468). JCC is supported by the NASA Space Technology Research Fellowship (NNX15AQ75H). Any opinions, findings, and conclusions or recommendations expressed in this material are those of the authors and do not necessarily reflect the views of the National Aeronautics and Space Administration or the National Science Foundation.

References

[1] R.F. Shepherd, F. Ilievski, W. Choi, S.A. Morin, A.A. Stokes, A.D. Mazzeo, X. Chen, M. Wang, G.M. Whitesides, Multigait soft robot, PNAS 108 (51) (2011) 20400–20403, http://dx.doi.org/10.1073/pnas.1116564108.

[2] E. Steltz, A. Mozeika, N. Rodenberg, E. Brown, H. Jaeger, JSEL: jamming skin enabled locomotion, in: IEEE/RSJ International Conference on Intelligent Robots and Systems, IROS 2009, 2009, pp. 5672–5677, http://dx.doi.org/10.1109/IROS.2009.5354790.

[3] S. Seok, C. Onal, K.-J. Cho, R. Wood, D. Rus, S. Kim, Meshworm: a peristaltic soft robot with antagonistic nickel titanium coil actuators, IEEE/ASME Trans. Mechatron. 18 (5) (2013) 1485–1497, http://dx.doi.org/10.1109/TMECH.2012.2204070.

[4] A.D. Marchese, R.K. Katzschmann, D. Rus, A recipe for soft fluidic elastomer robots, Soft Robot. 2 (1) (2015) 7–25, http://dx.doi.org/10.1089/soro.2014.0022.

[5] Y. Menguc, Y.-L. Park, E. Martinez-Villalpando, P. Aubin, M. Zisook, L. Stirling, R.J. Wood, C.J. Walsh, Soft wearable motion sensing suit for lower limb biomechanics measurements, in: 2013 IEEE International Conference on Robotics and Automation (ICRA), IEEE, 2013, pp. 5309–5316.

[6] J.T.B. Overvelde, Y. Menguc, P. Polygerinos, Y. Wang, Z. Wang, C.J. Walsh, R.J. Wood, K. Bertoldi, Mechanical and electrical numerical analysis of soft liquid-embedded deformation sensors analysis, Extreme Mech. Lett. 1 (2014) 42–46, http://dx.doi.org/10.1016/j.eml.2014.11.003.

[7] N. Cheng, M. Lobovsky, S. Keating, A. Setapen, K. Gero, A. Hosoi, K. Iagnemma, Design and analysis of a robust, low-cost, highly articulated manipulator

enabled by jamming of granular media, in: 2012 IEEE International Conference on Robotics and Automation (ICRA), 2012, pp. 4328–4333, http://dx.doi.org/10.1109/ICRA.2012.6225373.

[8] E. Brown, N. Rodenberg, J. Amend, A. Mozeika, E. Steltz, M.R. Zakin, H. Lipson, H.M. Jaeger, Universal robotic gripper based on the jamming of granular material, Proc. Natl. Acad. Sci. 107 (44) (2010) 18809–18814 arXiv:1009.4444.

[9] A. Jiang, G. Xynogalas, P. Dasgupta, K. Althoefer, T. Nanayakkara, Design of a variable stiffness flexible manipulator with composite granular jamming and membrane coupling, in: 2012 IEEE/RSJ International Conference on Intelligent Robots and Systems (IROS), 2012, pp. 2922–2927, http://dx.doi.org/10.1109/IROS.2012.6385696.

[10] R. Adam Bilodeau, E.L. White, R.K. Kramer, Monolithic fabrication of sensors and actuators in a soft robotic gripper, in: 2015 IEEE/RSJ International Conference on Intelligent Robots and Systems (IROS), IEEE, 2015, pp. 2324–2329.

[11] S. Ozel, N.A. Keskin, D. Khea, C.D. Onal, A precise embedded curvature sensor module for soft-bodied robots, Sens. Actuators A: Phys. 236 (2015) 349–356, http://dx.doi.org/10.1016/j.sna.2015.09.041.

[12] H.A. Wurdemann, S. Sareh, A. Shafti, Y. Noh, A. Faragasso, D.S. Chathuranga, H. Liu, S. Hirai, K. Althoefer, Embedded electro-conductive yarn for shape sensing of soft robotic manipulators, in: 2015 37th Annual International Conference of the IEEE Engineering in Medicine and Biology Society (EMBC), 2015, pp. 8026–8029, http://dx.doi.org/10.1109/EMBC.2015.7320255.

[13] N. Farrow, N. Correll, A soft pneumatic actuator that can sense grasp and touch, in: 2015 IEEE/RSJ International Conference on Intelligent Robots and Systems (IROS), 2015, pp. 2317–2323, http://dx.doi.org/10.1109/IROS.2015.7353689.

[14] R. Kramer, C. Majidi, R. Sahai, R. Wood, Soft curvature sensors for joint angle proprioception, in: 2011 IEEE/RSJ International Conference on Intelligent Robots and Systems (IROS), 2011, pp. 1919–1926, http://dx.doi.org/10.1109/IROS.2011.6094701.

[15] C. Majidi, R. Kramer, R.J. Wood, A non-differential elastomer curvature sensor for softer-than-skin electronics, Smart Mater. Struct. 20 (10) (2011) 105017, http://dx.doi.org/10.1088/0964-1726/20/10/105017.

[16] R. Kramer, C. Majidi, R. Wood, Wearable tactile keypad with stretchable artificial skin, in: 2011 IEEE International Conference on Robotics and Automation (ICRA), 2011, pp. 1103–1107, http://dx.doi.org/10.1109/ICRA.2011.5980082.

[17] F. Hammond, R. Kramer, Q. Wan, R. Howe, R. Wood, Soft tactile sensor arrays for micromanipulation, in: 2012 IEEE/RSJ International Conference on Intelligent Robots and Systems (IROS), 2012, pp. 25–32, http://dx.doi.org/10.1109/IROS.2012.6386224.

[18] H.-K. Lee, S.-I. Chang, E. Yoon, A flexible polymer tactile sensor: fabrication and modular expandability for large area deployment, J. Microelectromech. Syst. 15 (6) (2006) 1681–1686, http://dx.doi.org/10.1109/JMEMS.2006.886021.

[19] D.P.J. Cotton, I.M. Graz, S.P. Lacour, A multifunctional capacitive sensor for stretchable electronic skins, IEEE Sens. J. 9 (12) (2009) 2008–2009, http://dx.doi.org/10.1109/JSEN.2009.2030709.

[20] J.-B. Chossat, Y.-L. Park, R. Wood, V. Duchaine, A soft strain sensor based on ionic and metal liquids, IEEE Sens. J. 13 (9) (2013) 3405–3414, http://dx.doi.org/10.1109/JSEN.2013.2263797.

[21] J.-B. Chossat, H.-S. Shin, Y.-L. Park, V. Duchaine, Soft tactile skin using an embedded ionic liquid and tomographic imaging, J. Mech. Robot. 7 (2) (2015) 021008.

[22] J.-B. Chossat, Y. Tao, V. Duchaine, Y.-L. Park, Wearable soft artificial skin for hand motion detection with embedded microfluidic strain sensing, in: 2015 IEEE International Conference on Robotics and Automation (ICRA), 2015, pp. 2568–2573, http://dx.doi.org/10.1109/ICRA.2015.7139544.

[23] Y.-L. Park, B.-R. Chen, R.J. Wood, Design and fabrication of soft artificial skin using embedded microchannels and liquid conductors, IEEE Sens. J. 12 (8) (2012) 2711–2718, http://dx.doi.org/10.1109/JSEN.2012.2200790.

[24] T. Okuyama, M. Otsuki, R. Komiya, N. Sugoh, M. Tanaka, A curvature sensor using a solid polymer electrolyte, Int. J. Appl. Electromagn. Mech. 33 (1/2) (2010) 823–829.

[25] G. Alici, B. Mui, C. Cook, Bending modeling and its experimental verification for conducting polymer actuators dedicated to manipulation applications, Sens. Actuators A: Phys. 126 (2) (2006) 396–404, http://dx.doi.org/10.1016/j.sna.2005.10.020.

[26] K.M. Mossi, G.V. Selby, R.G. Bryant, Thin-layer composite unimorph ferroelectric driver and sensor properties, Mater. Lett. 35 (1–2) (1998) 39–49, http://dx.doi.org/10.1016/S0167-577X(97)00214-0.

[27] S. Baek, Y. Jeong, B. Lee, Characteristics of short-period blazed fiber bragg gratings for use as macro-bending sensors, Appl. Opt. 41 (4) (2002) 631, http://dx.doi.org/10.1364/AO.41.000631.

[28] B. Lee, S. Roh, J. Park, Current status of micro- and nano-structured optical fiber sensors, Opt. Fiber Technol. 15 (3) (2009) 209–221, http://dx.doi.org/10.1016/j.yofte.2009.02.006.

[29] K.S.C. Kuang, S.T. Quek, C.G. Koh, W.J. Cantwell, P.J. Scully, Plastic optical fibre sensors for structural health monitoring: a review of recent progress, J. Sens. 2009 (2009) e312053, http://dx.doi.org/10.1155/2009/312053.

[30] J. Albert, L.-Y. Shao, C. Caucheteur, Tilted fiber Bragg grating sensors, Laser Photon. Rev. 7 (1) (2013) 83–108, http://dx.doi.org/10.1002/lpor.201100039.

[31] M.A. Eddings, M.A. Johnson, B.K. Gale, Determining the optimal PDMS–PDMS bonding technique for microfluidic devices, J. Micromech. Microeng. 18 (6) (2008) 067001, http://dx.doi.org/10.1088/0960-1317/18/6/067001.

[32] E. White, J. Case, R. Kramer, Multi-element strain gauge modules for soft sensory skins, IEEE Sens. J. (2015) 1, http://dx.doi.org/10.1109/JSEN.2015.2507540.

[33] J.C. Case, E.L. White, R.K. Kramer, Soft material characterization for robotic applications, Soft Robot. 2 (2) (2015) 80–87, http://dx.doi.org/10.1089/soro.2015.0002.

Biographies

Edward L. White is a Ph.D. student in the Faboratory in the School of Mechanical Engineering at Purdue University, West Lafayette, IN, USA. He has an M.S. is mechanical engineering and an MBA from the University of Arizona, Tucson, AZ, USA. His research is focused on making soft robotic systems more manufacturerable and robust.

Jennifer C. Case is currently pursuing her Ph.D. degree in Mechanical Engineering from Purdue University, West Lafayette, IN, USA. She received her B.S. degree in Mechanical Engineering from Northern Illinois University, DeKalb, IL, USA, in 2013. Her research is focused on adding closed-loop control systems to highly deformable robots.

Rebecca K. Kramer is an Assistant Professor of Mechanical Engineering at Purdue University. She holds the degrees of B.S. from Johns Hopkins University, M.S. from the University of California at Berkeley, and Ph.D. from Harvard University. At Purdue, she founded The Faboratory, which contains a leading facility for the rapid design, fabrication, and analysis of materially soft and multifunctional robots. Her research interests include stretchable electronics, responsive material actuators, soft material manufacturing, and soft-bodied control. She is the recipient of the NSF CAREER Award, the NASA Early Career Faculty Award, the AFOSR Young Investigator Award, and was named to the 2015 Forbes 30 under 30 list.